



Cite this: *J. Mater. Chem. B*, 2023,
11, 5406

A photocatalytic carbon monoxide-generating effervescent microneedle patch for improved transdermal chemotherapy†

Junzhe Fu, Weijiang Yu, Xuedan Qian, Youxiang Wang * and Jian Ji *

Carbon monoxide (CO) is regarded as a promising therapeutic agent for chemotherapy sensitization. To simultaneously achieve controllable *in situ* CO production and efficient chemotherapeutics delivery is of great significance. Here, we presented a polyvinylpyrrolidone (PVP) core-shell microneedle (MN) system that encapsulated the effervescent component, photocatalyst, and doxorubicin hydrochloride (Dox-HCl) for CO-sensitized chemotherapy. Upon the insertion of MNs, the effervescent component, composed of sodium bicarbonate and tartaric acid, was exposed to interstitial fluid, leading to the burst release of carbon dioxide (CO₂). The generated gas not only enhanced the diffusion of Dox-HCl but also served as a substrate for the photocatalytic generation of CO. From the experimental results, the photocatalyst CuS atomic layers (CAL) displayed an effective CO₂ photoreduction performance, which could realize an irradiation time/intensity-dependent CO-controlled release. *Ex vivo* permeation studies demonstrated that effervescent CO₂ production markedly enhanced the intradermal diffusion of Dox-HCl. Eventually, the robust antitumor efficacy of this versatile MN platform was proved in B16F10-bearing nude mice. This CO-sensitized chemotherapeutic MN system offered a novel strategy for transdermal gas/drug delivery, which might provide a new direction in tumor suppression.

Received 30th November 2022,
Accepted 2nd March 2023

DOI: 10.1039/d2tb02613a

rsc.li/materials-b

10th Anniversary Statement

As a researcher who has been working in biomaterials for 30 years, I have had the great honor of serving as an associate editor of the *Journal of Materials Chemistry B* since 2018. I believe that our journal is on the right path and will be one of the leading journals for all bio-related materials. Besides the innovative conceptual research, we should pay more attention to those contributions which can be translated into real applications, such as implant and interventional medical devices, microneedle patches, advanced diagnostic systems and their combinations, *etc.* In an era of deep intersection of multiple disciplines, our journal should also welcome the integration of biomaterial research and more innovative technologies, such as big data technology, artificial intelligence, high-throughput experiment, 3D printing, stem cell and gene editing technology, to open up more possibilities in the future.

1. Introduction

Melanoma, a kind of tumor developing from melanocytes, is considered to be the most dangerous type of skin cancer. It is characterized by high malignancy, poor prognosis, and high mortality, which pose a serious threat to people's health and lives.^{1–3} In this regard, a series of anti-cancer treatments have been explored in depth. However, for classical drug delivery systems, the drug bioavailability of oral medication is often

limited by the first-pass metabolism while an intravenous injection also has a high degree of drug loss in the circulatory system.^{4,5} Microneedles (MNs) are an emerging drug delivery system developed in recent years. They are capable of overcoming the stratum corneum barrier and improving the transdermal efficiency of most drugs.^{6–10} The advantages of painless implementation and self-administration also make MNs exhibit an encouraging prospect in the field of drug delivery.^{11,12} In particular, MNs can be regarded as a more appealing platform for melanoma treatment.^{13–15} In terms of chemotherapy, MNs show great superiority over oral medication and intravenous injection owing to their substantial increase of drug bioavailability as well as the significant reduction of systemic toxicity. Nonetheless, MN-based chemotherapy is still limited by the low therapeutic efficiency of conventional chemotherapy agents.^{16–18}

MOE Key Laboratory of Macromolecule Synthesis and Functionalization,
Department of Polymer Science and Engineering, Zhejiang University, 310027,
P. R. China. E-mail: yx_wang@zju.edu.cn, jijian@zju.edu.cn

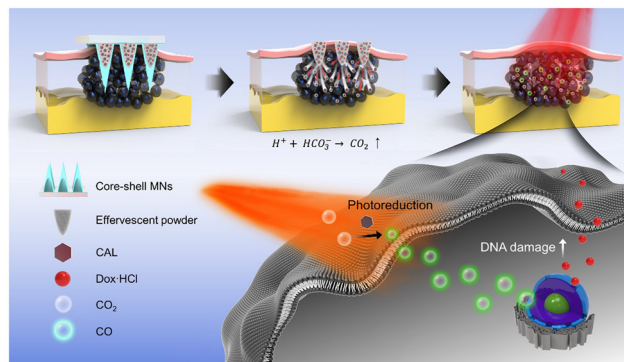
† Electronic supplementary information (ESI) available. See DOI: <https://doi.org/10.1039/d2tb02613a>

It is urgent to develop effective strategies and innovative designs for boosting the therapeutic performance of MN-mediated transdermal chemotherapy.

Carbon monoxide (CO), as one of the endogenous gaseous molecules, has drawn extensive attention in the realm of cancer treatment.¹⁹ As an important branch of gas therapy, CO can adjust the physiological or pathological tumor environment without drug resistance and adverse effects.^{20,21} Moreover, it has been proved that CO can substantially improve the therapeutic efficiency of chemotherapy.^{22–24} Given this, to achieve the safe administration of CO, a range of CO-releasing molecules (CORMs) have been reported.^{25,26} These CO donors are capable of carrying and releasing CO under certain stimuli but are still hampered by undesirable controllability and sensitivity. Recently, Zhang *et al.* proposed a concept of CO₂ photoreduction, using a photocatalytic nanomaterial (HisAgCCN) to transform CO₂ into CO for improving cancer therapy.²⁷ Compared with CORMs, such light-triggered CO generation endowed the strategy with higher responsiveness and accuracy, which might develop a new path for controllable CO administration.

Based on its unique advantages, CO₂ photoreduction may also afford a novel choice for transdermal chemotherapy sensitization. However, the cutaneous CO₂ content is likely to become a crucial factor hindering the efficiency of *in vivo* CO production. Effervescent tablets are an intriguing product of pharmaceutical and dietary industries. Upon coming in contact with water, the tablet will start disintegrating immediately and release a large amount of CO₂. It is a result of a chemical reaction that occurs between a carbonate or bicarbonate salt (*e.g.*, sodium bicarbonate) and a weak organic acid (*e.g.*, citric or tartaric acid).^{28,29} Through MN-based delivery, such an effervescent component can take effect in the presence of interstitial fluid. It may render a simple but distinctive way of achieving exogenous supplements for CO₂ photoreduction. More interestingly, the vigorous gas can provide an extra force to promote the delivery of other payloads in MNs, which has the potential to enhance the permeation and distribution of chemotherapeutics in the fibrotic tumor stroma.^{30–33}

Here, we presented a unique effervescent MN system for photocatalytic CO generation, endowed with controllable release of CO and enhanced permeation of chemotherapeutics for melanoma treatment (Scheme 1). The MN system was designed with a core-shell structure, consisting of a polyvinylpyrrolidone (PVP) shell and a mixed powder core. Among these, the mixed powder contained effervescent component sodium bicarbonate (NaHCO₃) and tartaric acid (C₄H₆O₆), CO₂ photoreduction catalyzer CuS atomic layers (CAL), and chemotherapy drug doxorubicin hydrochloride (Dox·HCl). When applying MNs to the lesions, with the dissolution of the PVP shell, the mixed powder was quickly exposed to the interstitial fluid. NaHCO₃ and C₄H₆O₆ would react instantaneously and lead to a rapid generation of CO₂. Once receiving 660 nm irradiation, CAL would transform CO₂ into CO *in situ*, which could significantly increase chemotherapeutic sensitivity. Additionally, the vigorous gas resulted in enhanced diffusion and deeper penetration depth of Dox·HCl to further improve the curative effect.



Scheme 1 Schematic illustration of photocatalytic CO-generating effervescent MNs for transdermal implantation and enhanced chemotherapy.

The photocatalytic performance of CAL was investigated *in vitro*. The drug diffusion behavior of effervescent MNs was studied in isolated skin tissue. The efficacy of CO-sensitized chemotherapy and its corresponding mechanism were explored in B16F10-bearing nude mice.

2. Experimental

2.1 Materials

Polyvinylpyrrolidone (PVP, $M_w = 360$ kDa) was purchased from Sigma-Aldrich (Shanghai, China). Sodium bicarbonate (NaHCO₃), DL-tartaric acid (C₄H₆O₆), doxorubicin hydrochloride (Dox·HCl), cuprous chloride (CuCl), oleylamine and octylamine were obtained from Aladdin (Shanghai, China). Sulfur (S) was purchased from Sinopharm Chemical Reagent (Shanghai, China). High-temperature resistance photosensitive resin master molds for MN fabrication (1400 μm height, 700 μm base width, 2 mm needle spacing, and 5 × 5 array) were provided by BMF Precision Tech (Shenzhen, China). Polydimethylsiloxane (PDMS, SYLGARD[®] 184 Silicone) was purchased from DOWSIL (USA). Optimum cutting temperature (OCT) compounds were purchased from Sakura Finetek (Hamacho, Japan). The phospho-histone H2A.X(Ser139) (γ-H2AX) rabbit monoclonal antibody and growth arrest and DNA damage-inducible 45A (GADD45A) rabbit polyclonal antibodies were obtained from Cell Signaling (Shanghai, China) and ABclonal (Wuhan, China), respectively.

2.2 Cell culture and animals

B16F10 and B16F10-LUC mouse melanoma cells were obtained from China Center for Type Culture Collection. The cells were cultured in Dulbecco's modified Eagle's medium (DMEM) supplemented with 1% (v/v) penicillin, 1% (v/v) streptomycin, and 10% (v/v) fetal bovine serum under a humidified atmosphere containing 5% CO₂ at 37 °C. Healthy female Balb/c nude mice (4 weeks old, weighing around 20 g) were provided by the Zhejiang Academy of Medical Sciences (Hangzhou, China). All animal experiments were carried out strictly according to the "Principles of Laboratory Animal Care" (NIH publication no. 86-23, revised 1985) and have received approval from the Lab Animal Welfare and Research Committee, Zhejiang University.

2.3 Synthesis and characterization of CAL

CAL was synthesized according to a previously reported procedure.³⁴ Specifically, CuCl (300 mg) was dispersed with 10 mL of octylamine and 10 mL of oleylamine in a three-necked flask. This mixture was heated at 100 °C for 0.5 h under flowing N₂ and then heated at 130 °C for 3 h. After that, S powder (288 mg) was mixed with 5 mL of octylamine and oleylamine, respectively, in another beaker and was subsequently added into the CuCl mixture with 5 h of heating at 95 °C. The as-obtained product was washed with ethanol and cyclohexane to remove organic residues. CAL was eventually obtained after vacuum drying. The successful synthesis of CAL was confirmed by X-ray diffraction analysis (X-pert powder, PANalytical B.V., Netherlands). The morphology of CAL was characterized using a scanning electron microscope (SEM, S-4800, Hitachi, Japan) and a transmission electron microscope (TEM, HT7700, Hitachi, Japan).

2.4 Hemoglobin assay

The CAL-catalyzed CO generation was quantitatively determined by the classical hemoglobin method.³⁵ Firstly, hemoglobin (4.2 μM final concentration) was dissolved in CO₂-saturated PBS and subsequently reduced by excess sodium dithionite. CAL (100 μg) was added to the reduced hemoglobin solution (1 mL). This system was rapidly sealed with liquid paraffin and then exposed to a 660 nm laser. After irradiation at different times or different intensities, the adsorption spectra of the solution were collected using a UV-vis absorption spectrometer (UV2600, Shimadzu, Japan). CO was detected by quantifying the conversion of hemoglobin (Hb) to carboxyhemoglobin (HbCO), which corresponded to the transition of the absorption bands from 430 nm to 410 nm. According to the Beer-Lambert law, the conversion of Hb to HbCO and the band intensity at 430 nm and 410 nm had the following quantitative relationships:

$$\frac{I_{410}}{I_{430}} = \frac{\varepsilon_{\text{Hb}(410)} \cdot a + \varepsilon_{\text{HbCO}(410)} \cdot b}{\varepsilon_{\text{Hb}(430)} \cdot a + \varepsilon_{\text{HbCO}(430)} \cdot b}$$

wherein, I_{410} and I_{430} represent the intensities of the collected spectrum at 410 nm and 430 nm; a and b are the relative proportion of Hb and HbCO in the system, assuming $a + b = 1$; $\varepsilon_{\text{Hb}(410)}$, $\varepsilon_{\text{Hb}(430)}$, $\varepsilon_{\text{HbCO}(410)}$ and $\varepsilon_{\text{HbCO}(430)}$ are molar extinction coefficients of Hb and HbCO at 410 nm and 430 nm in water, respectively.

Then the concentration of generated CO (C_{CO}) could be quantitatively calculated:

$$C_{\text{CO}} = 4.2\mu\text{M} \cdot b =$$

$$4.2\mu\text{M} \cdot \frac{\varepsilon_{\text{Hb}(430)} \cdot I_{410} - \varepsilon_{\text{Hb}(410)} \cdot I_{430}}{(\varepsilon_{\text{Hb}(430)} - \varepsilon_{\text{HbCO}(430)}) \cdot I_{410} - (\varepsilon_{\text{Hb}(410)} - \varepsilon_{\text{HbCO}(410)}) \cdot I_{430}}$$

wherein, $\varepsilon_{\text{Hb}(430)} = 528.6 \text{ mM}^{-1} \text{ cm}^{-1}$, $\varepsilon_{\text{Hb}(410)} = 304.0 \text{ mM}^{-1} \text{ cm}^{-1}$, $\varepsilon_{\text{Hb}(430)} - \varepsilon_{\text{HbCO}(430)} = 216.5 \text{ mM}^{-1} \text{ cm}^{-1}$, $\varepsilon_{\text{Hb}(410)} - \varepsilon_{\text{HbCO}(410)} = -442.4 \text{ mM}^{-1} \text{ cm}^{-1}$, which can be acquired from the tabulated molar extinction coefficient.

2.5 Photothermal properties of CAL

To evaluate the photothermal performance, CAL (100 μg) was added to CO₂-saturated PBS (1 mL) and then exposed to a 660 nm (or 808 nm) laser (0.4 W cm⁻², 5 min). The temperature was recorded using a NIR thermal imager (FLIR E60, FLIR Systems OU, Estonia).

2.6 Preparation and characterization of the core-shell MNs

The PDMS inverse mold was prepared by casting PDMS (base/curing agent(w/w) = 10:1) onto the master MN mold and cured at 80 °C. On this basis, the core-shell MNs were fabricated by a micro-molding technique. PVP aqueous solution (10% (w/v), 0.55 g) was firstly filled into the PDMS mold by centrifugation (5000 rpm, 5 min) and dried at 35 °C for 6 h. The shell of MNs with micro-cavity structures was thus obtained. To prepare the effervescent MNs, NaHCO₃ and C₄H₆O₄ were first mixed in a mole ratio of 2:1 to form the effervescent component. CAL (1 wt% of effervescent component) and Dox-HCl (5 wt% of effervescent component) were subsequently added and mixed thoroughly. Then the mixed powder (0.1 g) was centrifuged (5000 rpm, 3 min, 25 °C) to fill tightly into the micro-cavities. Finally, residual powder was removed with a spatula, and the powder-filled MN array was sealed with an adhesive base and peeled off from the mold for further use. For the non-effervescent MNs required for diffusion studies, the effervescent component was replaced with an equivalent PVP of low molecular weight ($M_w = 40 \text{ kDa}$), and the remaining steps were the same as above. For MNs with micro-cavities, no powder was added and the PVP shell was sealed with an adhesive base directly. The morphology of MNs was observed using a digital microscope and SEM. To further confirm the core-shell structure, the fluorescence images were photographed using a fluorescent inverted microscope (DS-Ri2, Nikon, Japan).

2.7 Mechanical strength and skin penetration tests

The mechanical strength of MNs was measured using an electro-mechanical tester (UTM5000, SUNS, China). The MN array was placed on the pallet of the testing machine and the force was continuously monitored when the top plate compressed the needles at a constant speed. The force-displacement curve was recorded.

The *in vitro* skin penetration test was performed. The effervescent MN patch was applied to isolated rat skin for 5 min, and the penetrating skin sample was instantly embedded in OCT compounds. The sample was frozen sectioned by cryotome (Cryostar NX50, Thermo, USA) and H&E staining was conducted. The H&E stained sample sections were observed under the bright field of a fluorescence microscope (TS2-S-SM, Nikon, Japan).

2.8 Drug diffusion studies

To evaluate the drug diffusion behavior of effervescent MNs, 1.5 wt% of agarose gel was used as an *in vitro* skin model, which was pierced by effervescent and non-effervescent MNs for different interval times (30 s, 1 min, and 2 min) and further cross-sectioned for analysis, respectively. Isolated porcine ear skin was pierced by effervescent and non-effervescent MNs for

20 min and immediately embedded in OCT compounds. After being frozen sectioned, the samples were observed using a fluorescence microscope.

2.9 *In vitro* cell viability and live/dead cell staining

To evaluate the *in vitro* cell-killing ability, the groups were firstly divided as follows: (1) no treatment (Control); (2) CAL (CAL); (3) CAL with laser irradiation (CAL(+)), representing the CO therapy group; (4) Dox-HCl and CAL (DOX + CAL), representing the chemotherapy therapy group; (5) Dox-HCl and CAL with laser irradiation (DOX + CAL(+)), representing the synergistic therapy group. For cytotoxicity assay, B16F10 cells were cultured in 96-well plates (8×10^3 cells per well) for 12 h and then given treatments (Dox-HCl: $2 \mu\text{g mL}^{-1}$, CAL: $100 \mu\text{g}$ per well, laser: 660 nm , 0.4 W cm^{-2} , 5 min). After incubation at 37°C for another 8 h, cells were tested by the CCK-8 assay to assess the cell viability. For live/dead cell staining, B16F10 cells were cultured in 24-well plates (1×10^5 cells per well) for 12 h and then given analogous treatments. The Calcein-AM/PI staining was performed. Cells stained green (alive) and red (dead) were imaged under a fluorescence microscope.

2.10 *In vivo* anti-tumor experiment

To establish the tumor model, female Balb/c nude mice were subcutaneously injected with B16F10-LUC cell suspensions (5×10^5 cells, $100 \mu\text{L}$) at the left outer thigh. After the tumor volume reached around 50 mm^3 , these B16F10-bearing nude mice were randomly divided into five groups ($n = 3$ per group): (1) no treatment (Control); (2) MNs loaded with CAL, NaHCO_3 and $\text{C}_4\text{H}_6\text{O}_4$ (CAL); (3) MNs loaded with CAL, NaHCO_3 and $\text{C}_4\text{H}_6\text{O}_4$ with laser irradiation (CAL(+)); (4) MNs loaded with Dox-HCl, CAL, NaHCO_3 and $\text{C}_4\text{H}_6\text{O}_4$ (DOX + CAL); (5) MNs loaded with Dox-HCl, CAL, NaHCO_3 and $\text{C}_4\text{H}_6\text{O}_4$ with laser irradiation (DOX + CAL(+)). The loading content of Dox-HCl and CAL in MNs was determined using UV-vis absorption spectrometry and inductively coupled plasma-optical emission spectrometer (ICP-OES, 730-ES, Varian, USA), respectively. All treatment groups received three times MN administration (laser: 660 nm , 0.4 W cm^{-2} , 5 min) on days 0, 3, and 6 and sacrificed on day 12. The tumor growth was monitored through *in vivo* bioluminescence and imaging (IVIS Spectrum, Xenogen, USA) on days 0, 3, 6, 9, and 12. Tumor volume ($\text{length} \times \text{width}^2 \times 1/2$) and body weight of mice were also recorded on days 0, 3, 6, 9, and 12 using a digital vernier caliper and scales, respectively. The isolated tumors were finally obtained on day 12 for weight measurement and then fixed with 4% (w/v) paraformaldehyde for H&E, immunohistochemistry (Ki67, TUNEL), and immunofluorescence ($\gamma\text{-H2AX}$, GADD45A) staining. The final tumor inhibition efficacy for each group was calculated by the formula: tumor inhibition efficacy = $(1 - W_1/W_2) \times 100\%$. W_1 refers to the excised tumor weight of the treated groups and W_2 refers to the excised tumor weight of the untreated group.

2.11 Statistics

For this study, all values in this study were analyzed by the unpaired *t*-test. Statistical differences were considered to be significant when $*p < 0.05$.

3. Results and discussion

3.1 Characterization of CAL

To build a photocatalytic CO_2 -generating MN system, the catalyzer of CO_2 photoreduction was first explored. CAL, an ultrathin conductor system, was introduced to transform CO_2 into CO under laser irradiation, which had great potential for spatiotemporally controllable CO generation. CAL was successfully synthesized according to the reported procedure.³⁴ From the SEM and TEM images shown in Fig. 1A and B, the hexagonal sheet-like structures of CAL were observed with a size of about 200 nm. Such nanostructures gave CAL a special partially occupied band. It could satisfy the band edge position for photoreduction potentials of CO_2 to CO. Moreover, the XRD pattern for CAL in Fig. 1C matched well with the diffraction patterns of hexagonal phase CuS (JCPDS Card No. 78-0877), proving the successful synthesis of CAL.

To further verify the CO_2 photoreduction performance of CAL, a classical hemoglobin assay was used to detect the generation of CO. Theoretically, CO could bind to the Fe(II) center in the reduced hemoglobin and then transform it into carboxyhemoglobin, corresponding to the transition of the absorption bands from 430 nm to 410 nm.³⁵ As shown in Fig. 1D, when CAL was added to saturated CO_2 solution and irradiated under 660 nm, the band at 430 nm was gradually decreased, while the intensity of the carboxyhemoglobin band at 410 nm was progressively increased, indicating the successful generation of CO. The CO production rate could also be quantified through this method (Fig. 1E). With a 5 min irradiation under 0.4 W cm^{-2} , the yield of CO reached $4.42 \mu\text{M}$. The quantitative relationship between CO generation and the irradiation intensity was detected in the same way (Fig. S1, ESI[†]). Additionally, CAL showed negligible photothermal performance under 660 nm irradiation (Fig. S2, ESI[†]). Therefore, CAL could be considered as an effective photocatalyst under 660 nm irradiation and the CAL-catalyzed CO generation could be precisely controlled by laser irradiation.

3.2 Design and characterization of the core-shell MNs

The core-shell MNs consisted of a PVP shell and a special core filled with mixed powder. The MNs were fabricated by the micro-molding technique (Fig. 2A). After filling PVP aqueous solution into the inverse mold and conducting drying, micro-cavities were obtained due to the shrinkage of PVP solution. Then the mixed powder— NaHCO_3 , $\text{C}_4\text{H}_6\text{O}_4$, CAL, and Dox-HCl were centrifugally loaded into the micro-cavities, and the effervescent MN array was finally sealed and peeled off through an adhesive base. As shown in Fig. 2B, the MNs had clear needle shapes with $\sim 1400 \mu\text{m}$ height, $\sim 700 \mu\text{m}$ base width, and $\sim 2 \text{ mm}$ needle spacing, which matched well with the specification of the master mold. The structure of concave micro-cavity could also be observed from the SEM image directly (Fig. 2C). In particular, the volume of the micro-cavity could be easily controlled. With the concentration of PVP solution increasing from 5% (w/v) to 20% (w/v), the volume of MNs' micro-cavity would decrease significantly (Fig. S3, ESI[†]). The PVP concentration of 10% (w/v) was ultimately chosen for the subsequent preparation of MNs. Fig. 2D and E show photographs

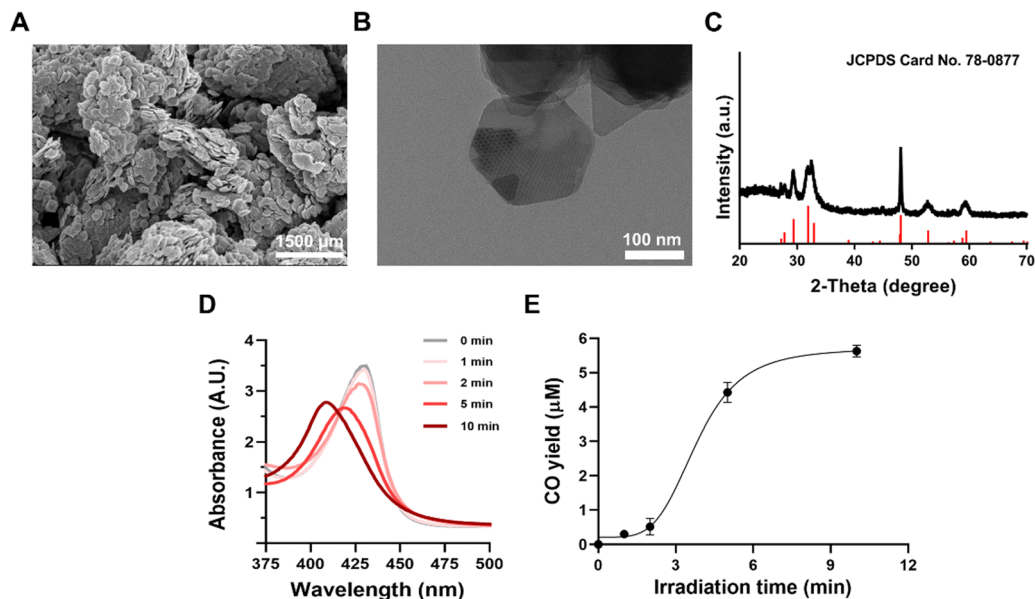


Fig. 1 The characterization of CAL. (A) SEM image, (B) TEM image, and (C) XRD pattern of CAL. (D) Hemoglobin assay for detecting CAL-catalyzed CO evolution and (E) corresponding CO yield, under 0.4 W cm^{-2} 660 nm irradiation, $n = 3$.

of MNs with micro-cavities and effervescent MNs, respectively. To further confirm the core-shell structure, the morphology of effervescent MNs was subsequently observed using the fluorescence microscope. As shown in Fig. 2F, the inner mixed powder was tightly filled into the micro-cavities. This core-shell design built a concept of “MN capsules”, which provided a feasible scheme for the loading and transdermal delivery of solid preparations. Moreover, the drug loading could be easily controlled by the volume of MNs’ micro-cavities as well as the proportion of multi-components.

For successful transdermal drug delivery, MNs should have sufficient mechanical strength to penetrate the stratum corneum barrier. In this regard, a mechanical compression test was conducted on solid PVP MNs, MNs with cavities, and effervescent MNs. As shown in Fig. 2G, MNs with micro-cavities exhibited an obvious yield during compression compared with solid PVP MNs, which was ascribed to the collapse of the micro-cavity structure. In comparison, the mechanical strength of effervescent MNs was slightly improved after the first yielding, which was probably due to the compaction of the powder core. Of note, these MNs have a similar compression curve before the displacement of 0.75 mm. Previous studies have indicated that the minimum force required to penetrate human skin is 0.058 N.³⁶ According to the force-displacement curve, the fracture force of all MNs met the requirement for skin penetration. Further experiments were performed *ex vivo* in isolated rat skin, the histological section indicated the successful penetration of rat stratum corneum (Fig. 2H). Collectively, these results demonstrated its ability to deliver the drug transdermally.

3.3 Drug diffusion behavior

NaHCO_3 and $\text{C}_4\text{H}_6\text{O}_4$, the main components of effervescent tablets, were innovatively introduced and encapsulated in MNs.

The CO_2 release process of effervescent MNs was first monitored using a digital microscope. As shown in Fig. 3A, after getting in contact with PBS solution, the PVP shell dissolved rapidly within 20 s. Uniformly mixed NaHCO_3 and $\text{C}_4\text{H}_6\text{O}_4$ reacted immediately and resulted in a rapid and excess release of CO_2 in 1 min, which would provide sufficient reactant for CO_2 photoreduction.

Besides serving as a substrate, such explosive release of CO_2 could make a great difference to promote drug diffusion in melanoma tissue. To verify the prompted migration of Dox-HCl, the diffusion behavior was assessed in the hydrogel model and isolated porcine ear skin, respectively. The effervescent MNs and non-effervescent MNs were prepared with the same loading content of Dox-HCl and simultaneously inserted into the agarose gel (Fig. 3B). The digital microscope images taken at different time intervals (30 s, 60 s and 120 s) confirmed the faster diffusion of Dox-HCl under the effervescence (Fig. 3C). Such improved permeation has been pronounced enough within 1 min, where effervescent MNs led to an average penetration depth of 1505.3 μm at 60 s *versus* only 357.3 μm value observed with non-effervescent MNs (Fig. S4, ESI†). Moreover, the distribution of Dox-HCl on pierced porcine ear skin is presented in Fig. 3D. With effervescent MNs pierced, Dox-HCl showed a significantly accelerated permeation, while the Dox-HCl delivered by non-effervescent MNs displayed negligible diffusion after 20 min. These results demonstrated that the vigorous release of CO_2 could markedly enhance the intradermal diffusion of Dox-HCl, which could be expected to improve the drug distribution in rigid tumor tissues.

3.4 *In vitro* cytotoxicity effect

The photocatalytic CO-generating effervescent MNs were designed to co-deliver CO and chemotherapy drugs for synergistic

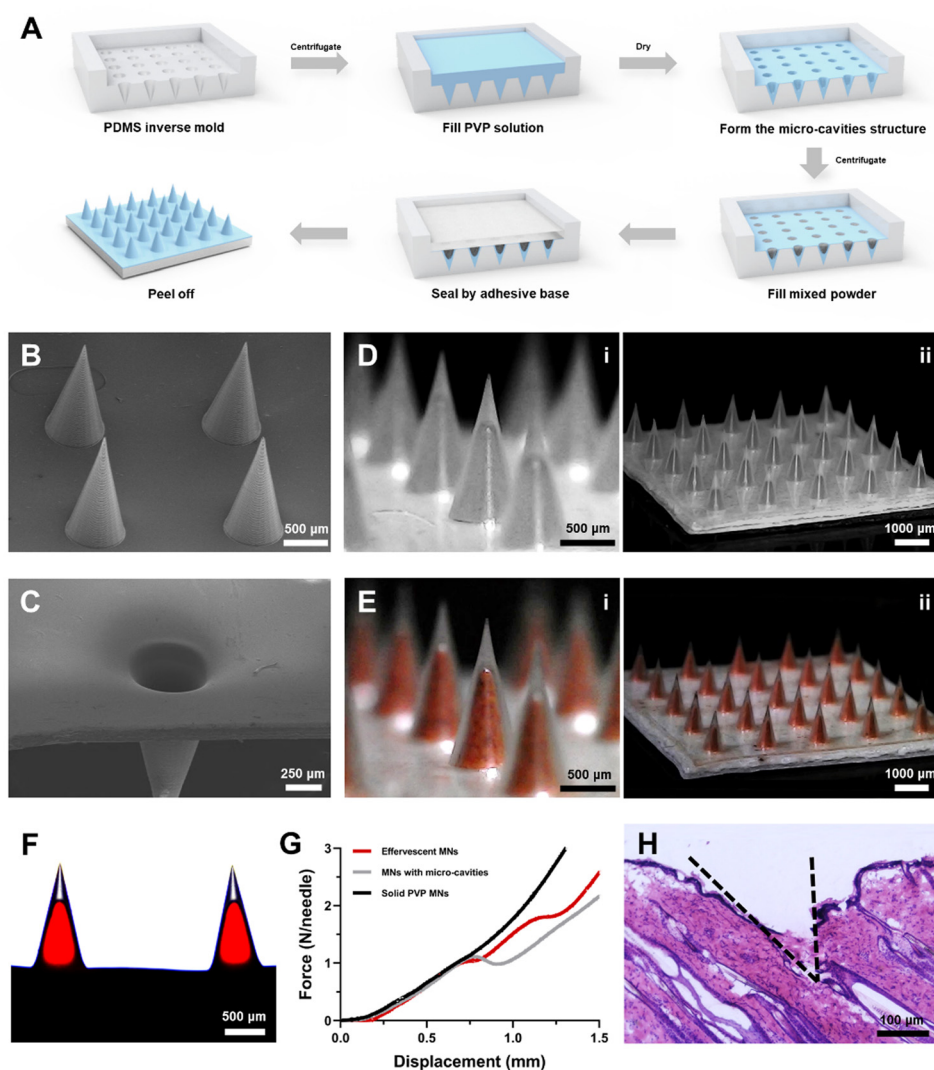


Fig. 2 The fabrication and characterization of MNs. (A) Fabrication process of core-shell MNs. (B and C) SEM images of the MN array and MN's micro-cavity structure, respectively. Photographs of (D) MNs with micro-cavities and (E) effervescent MNs. (F) Fluorescence image of representative effervescent MNs (merge: bright field + Dox-HCl displayed red fluorescence). (G) Compression force versus displacement plots of solid PVP MNs, MNs with micro-cavities, and effervescent MNs. (H) H&E staining of effervescent MNs penetrated rat skin.

melanoma treatment. Taking B16F10 mouse melanoma cells as a model, the anticancer effects of the scheme were first evaluated *in vitro*. The B16F10 cells were divided into five groups: no treatment (Control); CAL (CAL); CAL with laser irradiation (CAL(+)); Dox-HCl and CAL (DOX + CAL); and Dox-HCl and CAL with laser irradiation (DOX + CAL(+)). According to the photocatalytic performance of CAL, the irradiation condition was set to 660 nm, 400 mW cm⁻², 5 min. The result of the cytotoxicity effect is shown in Fig. 4A. No significant change in cell viability was observed in the CAL group. However, the cell viability dropped to 67.5% when a 660 nm laser irradiation was applied. In view of that the photothermal effect of CAL at this wavelength could be ignored, this result indicated certain anticancer effects of the generated CO. More importantly, compared with the DOX + CAL group, the cell survival rate of the DOX + CAL(+) group decreased sharply from 72.1% to 19.1%. The outstanding cell-killing effect of synergistic treatment could also be directly observed from the

Calcein AM/PI staining (Fig. 4B), which preliminarily proved the enhanced chemosensitivity by CO.

3.5 *In vivo* tumor growth inhibition

Motivated by promising results *in vitro*, the *in vivo* antitumor performance was then assessed. The treatment protocol is illustrated in the schematic shown as Fig. 5A. In detail, B16F10-bearing nude mice (implanted with B16F10-LUC cells) were randomly divided into five groups: no treatment (Control); MNs loaded with CAL, NaHCO₃ and C₄H₆O₄ (CAL); MNs loaded with CAL, NaHCO₃ and C₄H₆O₄ with laser irradiation (CAL(+)); MNs loaded with Dox-HCl, CAL, NaHCO₃ and C₄H₆O₄ (DOX + CAL); and MNs loaded with Dox-HCl, CAL, NaHCO₃ and C₄H₆O₄ with laser irradiation (DOX + CAL(+)). The loading content of Dox-HCl and CAL in MNs was determined using UV-vis spectroscopy and ICP-OES, and found to be 62.6 μg per patch and 18.0 μg per patch, respectively. The irradiation

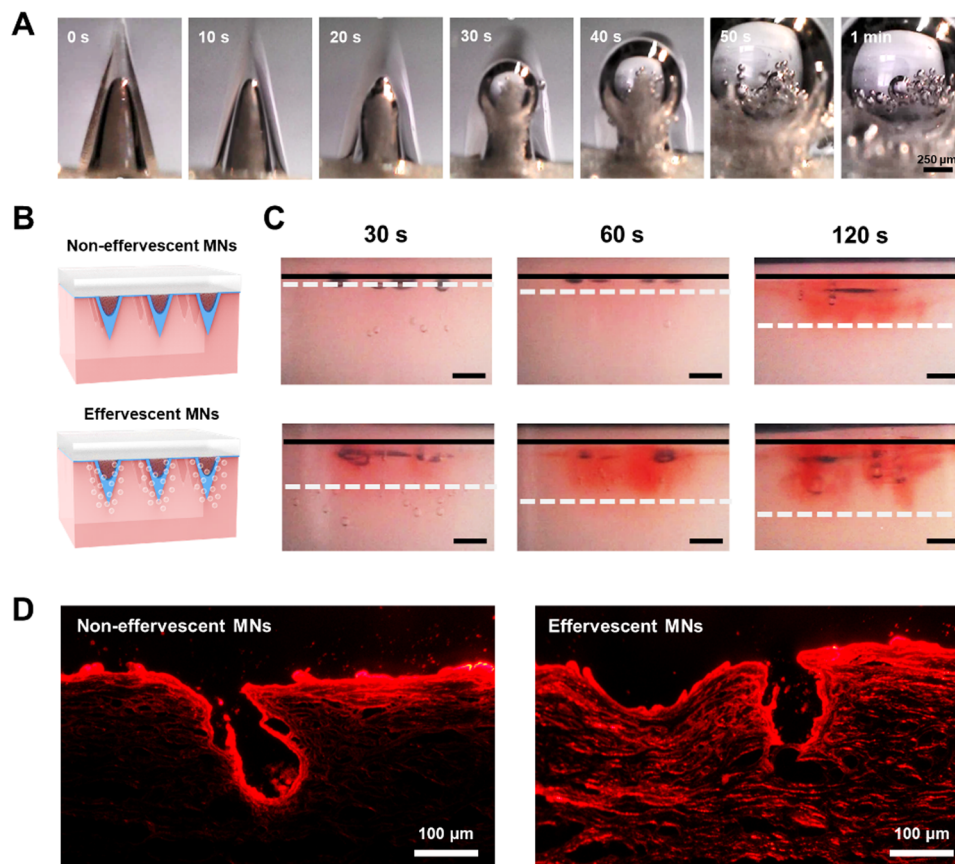


Fig. 3 The evaluation of *in vitro* and *ex vivo* drug release performance of effervescent MNs. (A) Dissolution process of a single effervescent MN tip (CAL and Dox-HCl) in PBS taken using a digital microscope (10 s intervals). (B) Schematic illustration set up of effervescent and non-effervescent MNs penetrating the hydrogel model. (C) Digital microscopy cross-section images of MNs inserting agarose gel (1.5 wt%) for 30 s, 60 s, and 120 s (scale bar: 1000 μm). (D) Fluorescence cross-section images of MNs inserting isolated porcine ear skin for 20 min (red: Dox-HCl).

settings were consistent with the parameters *in vitro* (660 nm , 400 mW cm^{-2} , 5 min). All treatment groups received 3 times of MN administration on days 0, 3 and 6. The body weight and tumor volume were recorded for 12 days.

The growth process of tumors was visualized by the bioluminescence signals of B16F10-LUC cells (Fig. 5B), and Fig. 5C shows the image of isolated tumors on day 12. Simultaneously, the antitumor efficacy was assessed by tumor volume (Fig. 5D)

and isolated tumor weight (Fig. 5E). The final tumor volume in the CAL group (1017 mm^3) was roughly similar to the Control group (1043 mm^3), proving the biocompatible implementation of CAL. The tumor growth was partly inhibited in the CAL(+) group and the DOX + CAL group, but still finally reached 269 mm^3 and 320 mm^3 (anti-tumor efficiency of 61.4% and 59.4%) respectively. The DOX + CAL(+) group exhibited the best antitumor effect, in which tumor growth was significantly

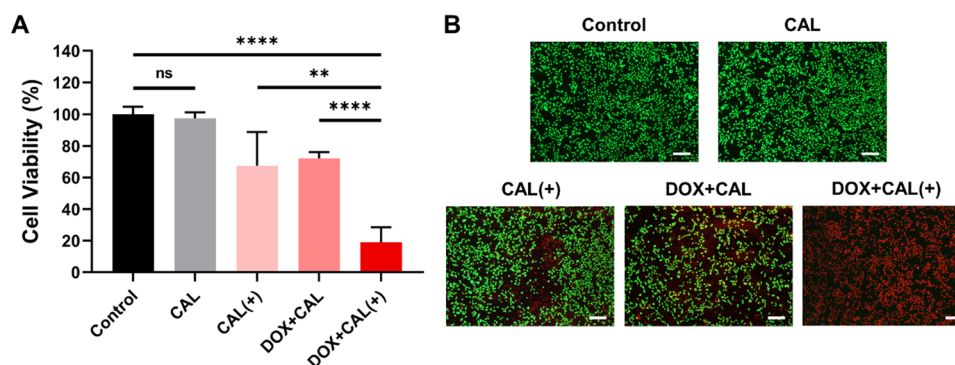


Fig. 4 *In vitro* cytotoxicity evaluation of CO-sensitized chemotherapy. (A and B) Cytotoxicity effect of B16F10 cells after different treatments: (A) cell viability ($n = 5$) and (B) Calcein-AM/PI staining (scale bar: $10\text{ }\mu\text{m}$). ns, $p > 0.05$, ** $p < 0.01$, **** $p < 0.0001$.

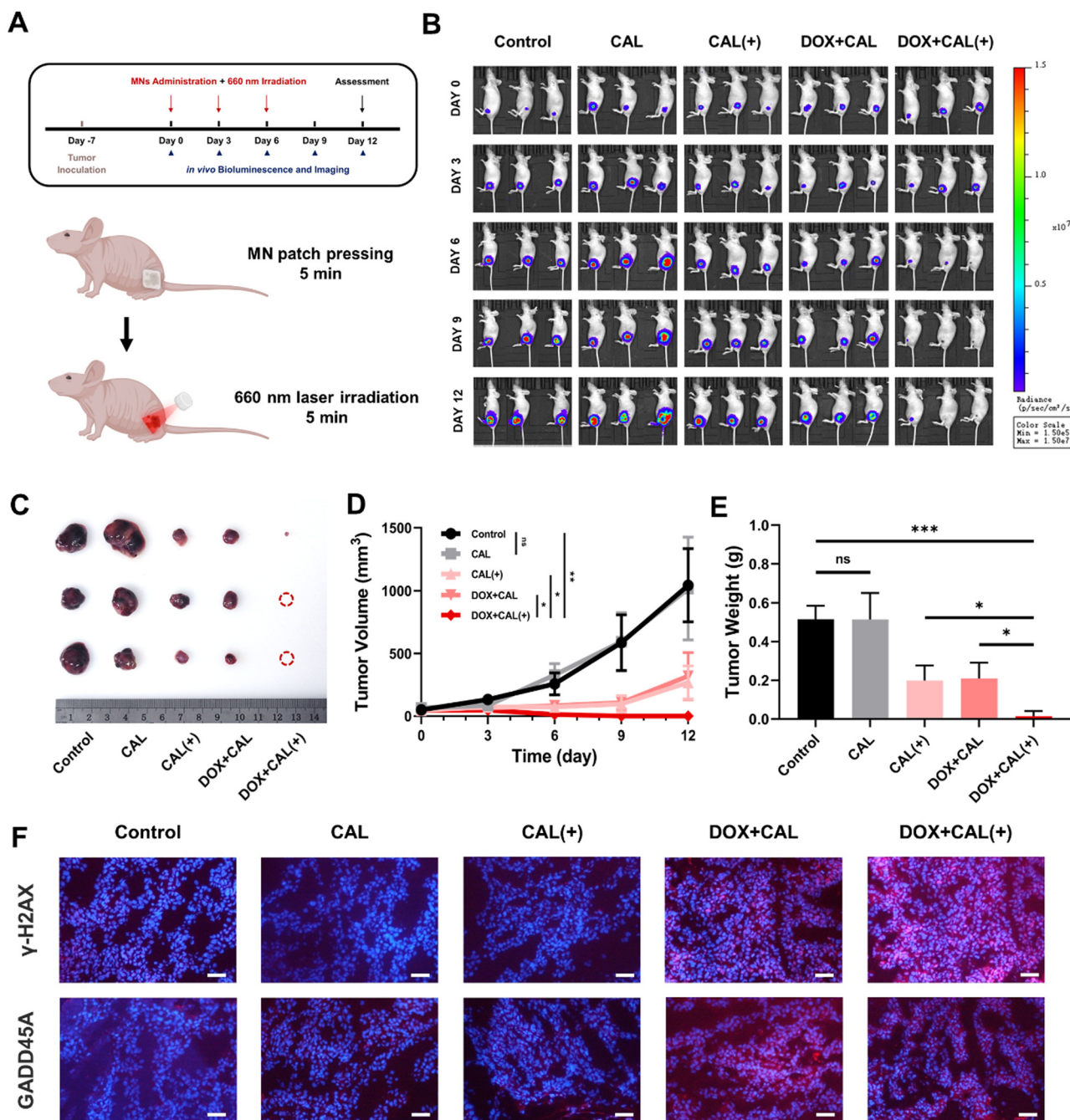


Fig. 5 *In vivo* antitumor evaluation of CO-sensitized chemotherapeutic MNs in B16F10-bearing nude mice. (A) Schematic illustration of the treatment protocol for MN application. (B) *In vivo* bioluminescence imaging of the B16F10 tumors of each group on days 0, 3, 6, 9, and 12 ($n = 3$). (C) Photographs of excisional tumors of each group on day 12. (D) Relative tumor volume changes during different treatments. (E) Tumor weights of each group on day 12. (F) Immunofluorescence staining of tumors of each group (red: γ -H2AX/GADD45A, blue: nucleus, scale bar: 10 μ m). ns, $p > 0.05$, * $p < 0.05$, ** $p < 0.01$, *** $p < 0.001$.

inhibited and even completely cured (anti-tumor efficiency of 97.1%). H&E, Ki67 and TUNEL immunohistochemical staining of the tumor showed the lowest tumor cell density, slowest cell proliferation and highest cell apoptosis in the DOX + CAL(+) group, further confirming the effective synergistic effect (Fig. S5, ESI[†]). Body weight remained stable during the 12 day treatment, which illustrated the good health conditions of treated mice (Fig. S6, ESI[†]). Additionally, compared with the DOX +

CAL group, the expressions of higher γ -H2AX (phospho-histone H2A.X, a marker of DNA double-strand breaks) and re-lowered GADD45A (growth arrest and DNA damage-inducible 45, related to DNA repair) were observed in the DOX + CAL(+) group (Fig. 5F). It is well known that doxorubicin, a typical topoisomerase II poison, exerts an antitumor effect by the production of double-strand DNA breaks.^{37–39} It has been reported that the enhanced DNA repair is one of the mechanisms for

doxorubicin to acquire resistance and further leads to low therapeutic efficiency for cancer chemotherapy.^{40–42} The presence of CO successfully inhibited DNA repair of tumor cells after Dox-HCl treatment and resulted in significantly aggravated DNA damage, which could become a powerful proof and reasonable explanation of the excellent therapeutic effectiveness of CO-sensitized chemotherapy.

4. Conclusions

In summary, we introduced a photocatalytic CO-generating effervescent MN system for effective CO-sensitized chemotherapy to treat melanoma. The MNs with a core-shell structure were successfully fabricated by a micro-molding method. Through the fast dissolution of the PVP shell, the effervescent component NaHCO₃ and C₄H₆O₆ could react rapidly in the environment of interstitial fluid. The generated CO₂ not only provided sufficient reactant for CAL-catalyzed CO generation but also substantially promoted the permeation of chemotherapy drug Dox-HCl, which could jointly help to improve the effectiveness of chemotherapeutic melanoma treatment. This versatile MN system exhibited excellent synergistic effects to inhibit B16F10 tumor growth *in vivo*. Overall, this photocatalytic CO-generating effervescent MN platform offered a promising strategy for CO-sensitized chemotherapy, which would provide a new insight into co-therapies to fight cancer.

Author contributions

Junzhe Fu: conceptualization, methodology, validation, formal analysis, investigation, data curation, and writing – original draft. Weijiang Yu: methodology, validation, formal analysis, investigation, and writing – review & editing. Xuedan Qian: investigation and data curation. Youxiang Wang: supervision, writing – review & editing, and funding acquisition. Jian Ji: supervision, project administration, writing – review & editing, and funding acquisition.

Conflicts of interest

There are no conflicts of interest to declare.

Acknowledgements

This work was financially supported by the National Key Research and Development Program of China (2020YFE0204400) and the National Natural Science Foundation of China (51873186).

References

- M. H. Pourhanifeh, M. Mahdavinia, R. J. Reiter and Z. Asemi, *J. Cell. Physiol.*, 2019, **234**, 12142–12148.
- D. Schadendorf, A. C. van Akkooi, C. Berking, K. G. Griewank, R. Gutzmer, A. Hauschild, A. Stang, A. Roesch and S. Ugurel, *Lancet*, 2018, **392**, 971–984.
- A. J. Miller and M. C. Mihm Jr., *N. Engl. J. Med.*, 2006, **355**, 51–65.
- J. B. Wolinsky, Y. L. Colson and M. W. Grinstaff, *J. Controlled Release*, 2012, **159**, 14–26.
- D. Liu and D. T. Auguste, *J. Controlled Release*, 2015, **219**, 632–643.
- Q. Bian, L. Huang, Y. Xu, R. Wang, Y. Gu, A. Yuan, X. Ma, J. Hu, Y. Rao and D. Xu, *ACS Nano*, 2021, **15**, 19468–19479.
- S. Huang, H. Liu, S. Huang, T. Fu, W. Xue and R. Guo, *Carbohydr. Polym.*, 2020, **246**, 116650.
- K. Tran, T. D. Gavitt, N. J. Farrell, E. J. Curry, A. B. Mara, A. Patel, L. Brown, S. Kilpatrick, R. Piotrowska and N. Mishra, *Nat. Biomed. Eng.*, 2021, **5**, 998–1007.
- C. Wang, Y. Ye, G. M. Hochu, H. Sadeghifar and Z. Gu, *Nano Lett.*, 2016, **16**, 2334–2340.
- A. Yuan, F. Xia, Q. Bian, H. Wu, Y. Gu, T. Wang, R. Wang, L. Huang, Q. Huang and Y. Rao, *ACS Nano*, 2021, **15**, 13759–13769.
- A. J. Guillot, A. S. Cordeiro, R. F. Donnelly, M. C. Montesinos, T. M. Garrigues and A. Melero, *Pharmaceutics*, 2020, **12**, 569.
- D. Zhi, T. Yang, T. Zhang, M. Yang, S. Zhang and R. F. Donnelly, *J. Controlled Release*, 2021, **335**, 158–177.
- K. Ita, *Biomed. Pharmacother.*, 2017, **93**, 1116–1127.
- W. Yu, X. Li, Y. Huang, Y. Chen, Q. Gao, Y. Wang and J. Ji, *Biomater. Sci.*, 2021, **9**, 4737–4745.
- X. Li, Q. Xu, P. Zhang, X. Zhao and Y. Wang, *J. Controlled Release*, 2019, **314**, 72–80.
- J. Shi, P. W. Kantoff, R. Wooster and O. C. Farokhzad, *Nat. Rev. Cancer*, 2017, **17**, 20–37.
- R. Agarwal and S. B. Kaye, *Nat. Rev. Cancer*, 2003, **3**, 502–516.
- G. Housman, S. Byler, S. Heerboth, K. Lapinska, M. Longacre, N. Snyder and S. Sarkar, *Cancers*, 2014, **6**, 1769–1792.
- S. H. Heinemann, T. Hoshi, M. Westerhausen and A. Schiller, *Chem. Commun.*, 2014, **50**, 3644–3660.
- R. Motterlini and L. E. Otterbein, *Nat. Rev. Drug Discovery*, 2010, **9**, 728–743.
- Y. Zhou, W. Yu, J. Cao and H. Gao, *Biomaterials*, 2020, **255**, 120193.
- S.-B. Wang, C. Zhang, Z.-X. Chen, J.-J. Ye, S.-Y. Peng, L. Rong, C.-J. Liu and X.-Z. Zhang, *ACS Nano*, 2019, **13**, 5523–5532.
- Y. Li, J. Dang, Q. Liang and L. Yin, *ACS Cent. Sci.*, 2019, **5**, 1044–1058.
- X. Yao, P. Yang, Z. Jin, Q. Jiang, R. Guo, R. Xie, Q. He and W. Yang, *Biomaterials*, 2019, **197**, 268–283.
- J. Boczkowski, J. J. Poderoso and R. Motterlini, *Trends Biochem. Sci.*, 2006, **31**, 614–621.
- C. C. Romão, W. A. Blättler, J. D. Seixas and G. J. Bernardes, *Chem. Soc. Rev.*, 2012, **41**, 3571–3583.
- D. W. Zheng, B. Li, C. X. Li, L. Xu, J. X. Fan, Q. Lei and X. Z. Zhang, *Adv. Mater.*, 2017, **29**, 1703822.
- A. Advankar, R. Maheshwari, V. Tambe, P. Todke, N. Raval, D. Kapoor and R. K. Tekade, in *Drug Delivery Systems*, Elsevier, 2019, pp. 615–664.

- 29 A. Awad, A. Goyanes, A. Basit, A. Zidan, C. Xu, D. Li, R. Narayan and R. K. Chen, *J. Manuf. Sci. Eng.*, 2022, 1–71.
- 30 M. A. Lopez-Ramirez, F. Soto, C. Wang, R. Rueda, S. Shukla, C. Silva-Lopez, D. Kupor, D. A. McBride, J. K. Pokorski and A. Nourhani, *Adv. Mater.*, 2020, **32**, 1905740.
- 31 S. Kusama, K. Sato, Y. Matsui, N. Kimura, H. Abe, S. Yoshida and M. Nishizawa, *Nat. Commun.*, 2021, **12**, 1–11.
- 32 K. C. Valkenburg, A. E. De Groot and K. J. Pienta, *Nat. Rev. Clin. Oncol.*, 2018, **15**, 366–381.
- 33 P. Queirolo and F. Spagnolo, *Cancer Treat. Rev.*, 2017, **59**, 71–78.
- 34 X. Li, L. Liang, Y. Sun, J. Xu, X. Jiao, X. Xu, H. Ju, Y. Pan, J. Zhu and Y. Xie, *J. Am. Chem. Soc.*, 2018, **141**, 423–430.
- 35 Q. He, D. O. Kiesewetter, Y. Qu, X. Fu, J. Fan, P. Huang, Y. Liu, G. Zhu, Y. Liu and Z. Qian, *Adv. Mater.*, 2015, **27**, 6741.
- 36 J.-H. Park, M. G. Allen and M. R. Prausnitz, *J. Controlled Release*, 2005, **104**, 51–66.
- 37 G. Minotti, P. Menna, E. Salvatorelli, G. Cairo and L. Gianni, *Pharmacol. Rev.*, 2004, **56**, 185–229.
- 38 C. Carvalho, R. X. Santos, S. Cardoso, S. Correia, P. J. Oliveira, M. S. Santos and P. I. Moreira, *Curr. Med. Chem.*, 2009, **16**, 3267–3285.
- 39 G. Hortobagyi, *Drugs*, 1997, **54**, 1–7.
- 40 K. Cheung-Ong, G. Giaever and C. Nislow, *Chem. Biol.*, 2013, **20**, 648–659.
- 41 J. Liu, G. Jiang, P. Mao, J. Zhang, L. Zhang, L. Liu, J. Wang, L. Owusu, B. Ren and Y. Tang, *Sci. Rep.*, 2018, **8**, 1–11.
- 42 B. Wegiel, D. Gallo, E. Csizmadia, C. Harris, J. Belcher, G. M. Vercellotti, N. Penacho, P. Seth, V. Sukhatme and A. Ahmed, *Cancer Res.*, 2013, **73**, 7009–7021.